Near- and far-infrared absorption and electronic structure of Ge-SiGe multiple quantum wells

Y. Busby, M. De Seta, G. Capellini,* and F. Evangelisti

Dipartimento di Fisica, Università di Roma Tre, via Vasca Navale 84, I-00146 Roma, Italy

M. Ortolani

Istituto di Fotonica e Nanotecnologie, CNR, via Cineto Romano 42, I-00156 Roma, Italy

M. Virgilio and G. Grosso

NEST, Istituto Nanoscienze-CNR and Dipartimento di Fisica "E. Fermi," Università di Pisa, largo Pontecorvo 3, I-56127 Pisa, Italy

G. Pizzi

NEST, Istituto Nanoscienze-CNR, Scuola Normale Superiore, Piazza dei Cavalieri 7, I-56126 Pisa, Italy

P. Calvani

CNR-SPIN and Dipartimento di Fisica, Università di Roma La Sapienza, P.le A. Moro 2, I-00185 Roma, Italy

S. Lupi

CNR-IOM and Dipartimento di Fisica, Università di Roma La Sapienza, P.le A. Moro 2, I-00185 Roma, Italy

M. Nardone

Dipartimento di Fisica and CNISM-CNR, Università de L'Aquila, via Vetoio, 67100 Coppito, Italy

G. Nicotra and C. Spinella

CNR-IMM, Stradale Primosole 50, 95121 Catania, Italy

We report an extensive study of strained $Ge/Si_{0.2}Ge_{0.8}$ multiquantum wells grown by ultrahigh-vacuum chemical-vapor deposition. The microstructural properties of the samples were characterized by transmission electron microscopy and Raman spectroscopy. Their electronic properties have been investigated by means of infrared absorption measurements. Both interband and intersubband transitions were analyzed. Intersubband absorption energies were found in the 20–50 meV range, depending on the quantum well width. Interband and intersubband transition energies have been successfully described by means of both a $\mathbf{k} \cdot \mathbf{p}$ approach and a tight-binding model. In particular, we found a conduction-band offset between the L edges of 124 meV, well suited for the development of optoelectronic devices operating in the terahertz range. We also found that the energy difference between the Δ_2 minima in the barrier and the L minima in the well is only ~40 meV. This explains the observed ineffectiveness of the transfer doping in the strained heterostructures considered.

PACS number(s): 73.21.Fg, 68.65.Fg, 81.15.Gh

I. INTRODUCTION

The fabrication of heterostructures based on strained germanium (s-Ge) (001) quantum wells confined between $Si_{1-x}Ge_x$ layers of high Ge content ($0.75 < x < 1$) has recently attracted great interest for their potential in optoelectronic applications.[1] Due to the proximity of the direct and indirect gap, SiGe heterostructures with high Ge content are expected to exhibit optical properties similar to those of direct-gap systems.[2,3] Furthermore s-Ge wells have the conduction-band minimum at L and small confinement effective mass in the growth direction, resulting in strong intersubband transition strength. The presence of off-diagonal terms in the effective-mass tensor relaxes the TM polarization selection rule thus allowing in principle the use of a normal incidence geometry. Most important, the nonpolar character of the material reduces the influence of optical phonons on intersubband relaxation, as compared to similar devices made of III-V semiconductors. As a consequence, SiGe/Ge heterostructures are particularly promising systems for the devel-

opment of unipolar quantum cascade emitters operating at room temperature in the terahertz (THz) range.[1,4,5]

In order to achieve this aim, it is fundamental to acquire a precise knowledge of the bands lineup at the $Si_{1-x}Ge_x/Ge$ interface, a difficult task in the high Ge composition range. First of all, in relaxed $Si_{1-x}Ge_x$ alloys, the absolute conduction-band minimum has a $\Delta - L$ crossover at $x = 0.85$. Furthermore, the strain in the structure changes significantly the energy of all conduction-band minima. Given a layer sequence, it is therefore crucial to investigate the relative energy position of the Δ and L states in the strained barriers and wells. The more so since their relative energy position plays a crucial role in phenomena, such as carrier tunneling and transfer doping effectiveness, which underlies the performance of optoelectronic devices based on heterostructures.[4]

So far information on the SiGe/Ge band lineups was prevalently theoretical.[1–3,6] Indeed, most of the experimental work on SiGe heterostructures and on SiGe-based devices has been focused on alloys pseudomorphically grown on Si with a Ge mole fraction x in the range 0.20–0.50.[1,7–11] This

choice was mainly due to the difficulty of growing strained Ge-rich heterostructures on silicon, a process requiring, in order to avoid strain release, the presence of relaxed alloy buffer layers with high-Ge content. Recent progress in the growth of low-defect high-Ge content virtual substrates (VSs) (Refs. [12–15]) has opened the way to deposit high-quality quantum heterostructures based on high-Ge-content SiGe alloys.[5,12,16–19] Absorption and luminescence spectra of interband transitions in s-Ge multiquantum wells (MQWs), with type I band alignment, have been experimentally investigated.[17,20]

In a previous paper[5] we have presented experimental evidence of conduction-band intersubband transitions in compressively strained Ge quantum wells confined between Ge-rich SiGe barriers. Here, we report an extensive study of the structural and optical properties of doped as well as intrinsic s-Ge/$Si_{0.2}Ge_{0.8}$ MQWs, with well width in the range 8.5–24 nm. Thickness, interface roughness, and defect densities have been determined by means of transmission electron microscopy, strain, and composition of the different layers by Raman and x-ray photoemission spectroscopy (XPS). Both, interband and intersubband absorption measurements have been performed and interpreted by means of tight binding (TB) and $\mathbf{k} \cdot \mathbf{p}$ calculations. The observed features and the agreement between theoretical and experimental data demonstrate the high quality of the chemical-vapor deposition (CVD)-grown s-Ge MQWs, the presence of a significant conduction-band offset and the effectiveness of the adopted theoretical models for evaluating band profiles, electronic structures, and self-consistent spatial distribution of charge carriers due to transfer doping. Furthermore, the careful determination of the strain conditions of the heterostructures has allowed the evaluation of the relative position of the Δ and L minima in the barriers and in the wells.

II. EXPERIMENTAL

All the heterostructures have been grown by ultrahigh-vacuum chemical-vapor deposition from ultrapure silane and germane, without carrier gas. The process pressure was in the 10^{-3} Torr range while the system base pressure was in the low 10^{-10} Torr range. First of all, we have deposited on Si (001) substrates a reverse-graded VS comprising a 500 nm thick, plastically relaxed heteroepitaxial Ge layer followed by a 500-nm-thick $Si_{0.15}Ge_{0.85}$ layer deposited at a deposition temperature $T_{dep} = 500$ °C (further details on the VS growth can be found in Ref. [13]). On top of this VS we have deposited N_w sequences of strained Ge wells confined between *n*-doped $Si_{0.2}Ge_{0.8}$ barriers ($T_{dep} = 500$ °C). The doping has been obtained by codeposition, adding phosphine to the reacting gases. In selected samples, we have inserted a neutral SiGe spacer layer between the *n*-doped barriers and the Ge wells. On top of the multiquantum wells a 150-nm-thick $Si_{0.15}Ge_{0.85}$ cap layer has been deposited. The growth rate of the multiquantum well region was 0.1 nm s^{-1}.

The microstructural analysis of the heteroepitaxial layers has been performed by means of transmission electron microscopy, both in scanning mode and in cross section (STEM) (X). STEM analysis has been performed with a

JEOL 2010F TEM/STEM system equipped with a 200 kV Schottky field-emission electron gun, an ultrahigh-resolution objective lens pole piece with a small spherical aberration coefficient ($C_s = 0.5$ mm), a Gatan imaging filter, a Jeol STEM unit, a Jeol ADF detector, and a Gatan DIGISCAN. The STEM was operated in high angle annular dark field mode (HAADF).

The Raman spectra were collected by means of a "Labram" confocal micro-Raman setup by Jobin-Yvon operating with a $\lambda = 632$ nm excitation wavelength. The spectral resolution was 3 cm^{-1}. Absolute frequencies were calibrated using a Si standard and some plasma discharge lines of the He-Ne laser.

Low-temperature Fourier-transform IR measurements in the near-infrared (NIR) range have been performed in single pass transmission geometry with nonpolarized light at normal incidence. The low-temperature intersubband absorption spectra have been measured using a He-flow optical cryostat coupled to a rapid-scan Michelson interferometer. The transmitted radiation has been detected with a Si bolometer operating at 4.2 K. Since intersubband transitions are enhanced when the polarization vector for the electric field is parallel to the growth direction,[21] the incoming radiation has been coupled to the samples adopting a waveguide geometry with lateral facets at 45°. The facets as well as the back side of the samples have been optically polished and the top (growth) side has been coated with a 5-nm-thick Cr layer followed by an 80-nm-thick Au metallization. The waveguide length of the analyzed samples was ~ 5–6 mm, the total thickness 0.7 mm and, as a consequence, 3–4 double reflections occurred inside the waveguide. The incoming radiation was linearly polarized with a wire-grid polarizer. For each sample we have measured both the $T_E(\nu)$ transmitted spectra with the electric field polarized orthogonally to the growth axis and the $T_M(\nu)$ transmitted spectra, having a component along the growth axis. To account for the linear dichroic properties of the apparatus, $T_E(\nu)$ and $T_M(\nu)$ have been normalized using the $S_E^0(\nu)$ and $S_M^0(\nu)$ transmission spectra measured without samples in the cryostat.

In the vicinity of the Au-metallization layer where the active MQWs region is located, the component of the electric field parallel to the growth axis is enhanced while the one orthogonal to the growth axis is strongly suppressed by phase matching effects.[20] As a consequence, the intersubband transitions in the MQWs are present in the $T_M(\nu)$ spectra only and do not contribute to the $T_E(\nu)$ spectra. This effect can be exploited to distinguish the intersubband transition signal from other polarization-independent features present in the spectra, such as, for instance, the narrow lines related to the transitions among hydrogenlike levels of the dopants in the Si substrate (see Fig. 1 in Ref. [5]). To filter out such features, we have evaluated the dichroic transmission spectra $T_d(v) = T_M(v)/T_E(v)$.

III. EXPERIMENTAL RESULTS

A. Structural and morphological analyses

The characteristics of the samples investigated in this study are reported in Table I. The microstructural analysis of

TABLE I. Structural characteristics of the investigated samples: s-Ge well thickness d_w; the $Si_{0.2}Ge_{0.8}$ barrier thickness d_b (including spacer layer thickness d_s, when present); equivalent composition x_{eq} of a relaxed cubic alloy having the same in-plane lattice parameter $a_\parallel$ of the sample, as determined by Raman spectroscopy; donor density in the barriers N_D; number of quantum wells in the samples N_w.

Sample	d_w (nm)	d_b (nm)	d_s (nm)	x_{eq}	$a_\parallel$ (Å)	N_D (10^{18} cm^{-3})	N_w
1617	8.5	29.6	4+4			5.5	10
1630	10.0	22.5	0			0.85	10
1616	10.2	22.0	0			2.5	10
1619	12.0	28.0	4+4			5.5	10
1596	15.0	30.0	0	0.93	5.641	4.6	10
1594	18.5	30.0	0	0.93	5.641	4	10
1597	19.5	30.0	0	0.93	5.641	4.8	10
1598	24.0	30.0	0	0.93	5.641	4.8	8
1636	12.0	20.0	0	0.935	5.642	No	10
1593	17.0	27.3	0	0.935	5.641	No	10
1595	18.4	30.0	0			No	10
1638	19.0	19.0	0	0.95	5.645	No	30
1587	24.0	30.0	0	0.93	5.641	No	10

one of the samples performed by STEM in HAADF mode is shown in Fig. 1. In HAADF-STEM the sensitivity contrast is a function of the square of the atomic number Z. This feature, combined with the high spatial resolution typical of STEM, allows us to distinguish easily between layers of different composition, as can be observed in the figure. In particular, Fig. 1(b) demonstrates that a composition variation of $\sim5\%$ only, i.e., from $x=0.85$ in the VS to $x=0.8$ in the barrier, is clearly discerned. Barrier and well thickness fluctuations for a given MQW stack are within the 2% of the values given in Table I. The absence in Fig. 1(a) of extended defects such as threading dislocations and/or stacking faults (highly visible with the STEM) evidences the structural quality of the VS and of the active part of the sample (a detailed discussion on the VS can be found in Ref. 13).

The high Z-contrast sensitivity and the atomic resolution obtainable in HAADF-STEM configuration allowed us to measure the interface roughness in the multiquantum well region. The typical interfacial rms roughness was less than 0.4 nm [Fig. 1(c)]. We found that the interdiffusion was minimal and that the roughness at the interface was mainly due to the presence of abrupt monoatomic steps of SiGe in the Ge region and vice versa.

Surface topography has been studied with conventional atomic force microscopy (AFM), which has shown that typical rms roughness values were on the order of ~3 nm and that a density of 10^6-10^7 cm^{-2} pits was present in the cap layer, attributed to the influence of the threading dislocations on the growth[13] (see Fig. 2). Composition and strain of the samples have been investigated by means of Raman spectroscopy.

The Raman spectrum of a typical multilayered Ge/SiGe structure (top) together with that of a reference Ge(001) substrate (bottom) are reported in Fig. 3. The Ge/SiGe spectrum clearly show two peaks around 300 cm^{-1} and a third one
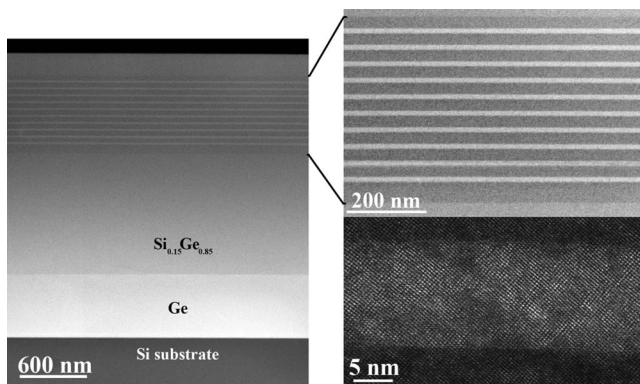

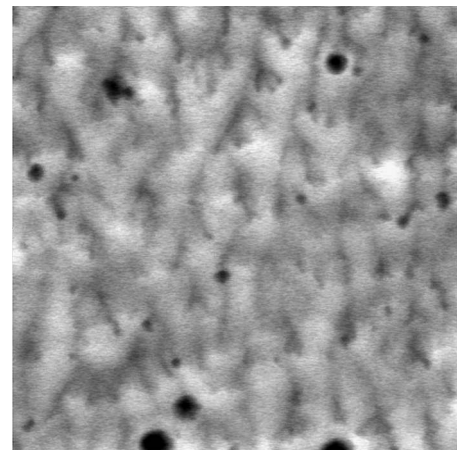FIG. 1. STEM-HAADF images of sample 1619 at increasing magnifications (specificare a,b,c).

FIG. 2. 25×25 μm^2 AFM image of a typical MQW sample. The height range is 35 nm. Image sides are aligned along the [011] directions.
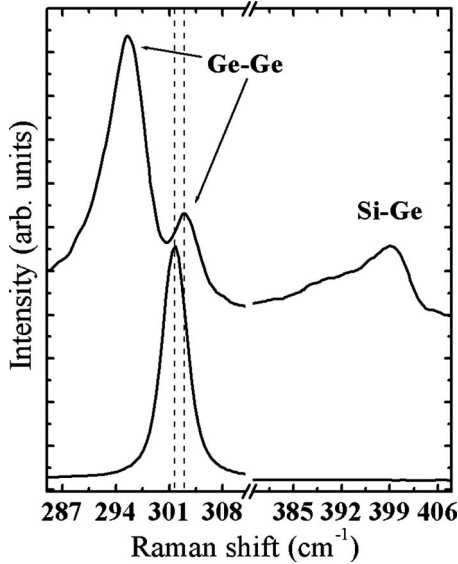
FIG. 3. (Top) Raman spectrum of the 1594 MQW sample in the spectral region of the Ge-Ge and Si-Ge vibration mode. (Bottom) Raman spectrum of a reference bulk Ge(001) substrate.
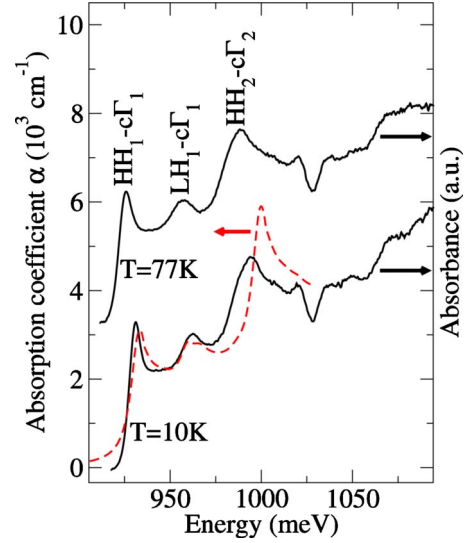

FIG. 4. (Color online) Interband absorbance spectra (right vertical axis) of the 1638 30MQWs sample measured at 10 and 77 K (black solid lines). The spectrum at $T = 77$ K has been displaced along the vertical axis for clarity. Peaks attribution and the low-temperature theoretical absorption spectrum (left vertical axis) are also shown (dashed line).

located at about 400 cm^{-1}. In agreement with the literature,[22] we have attributed these lines to the Ge-Ge vibration mode excited in the SiGe layers and in the Ge wells, and to the Si-Ge vibration mode, respectively. As a matter of fact, owing to the wavelength used in our Raman setup and the sample composition, the incident laser beam has an attenuation length of $\sim$50 nm. Consequently, the Raman signal is originated in the first layers of the stacked structure and no contribution to the spectra from the underlying Ge/Si substrate is observed.

The knowledge of the vibrational frequencies as obtained by the Raman spectroscopy enables the simultaneous determination of the composition x and the biaxial strain $\varepsilon_{\parallel}$ in Si$_{1-x}$Ge$_x$ heterostructures.[13,23] This can be done by solving the following system:

$$\omega_{\text{Si-Ge}}(x, \varepsilon_{\parallel}) = \omega_{\text{Si-Ge}}^0 + 24.5x - 4.5x^2 - 33.5x^3 + b_{\text{SiGe}}\varepsilon_{\parallel},$$

$$\omega_{\text{Ge-Ge}}(x, \varepsilon_{\parallel}) = \omega_{\text{Ge-Ge}}^0 + 19.4x + b_{\text{Ge}}\varepsilon_{\parallel}, \quad (1)$$

where the ω_i^0 are the mode frequencies in unstrained alloys with $x \to 0$, and b_i are phenomenological parameters dependent on the elastic constants of the material and are independent of x in the composition range considered in this work. Their values have been taken from Refs. 24 and 25. The compositions x obtained with this method are in agreement with those obtained by XPS, secondary-ion-mass spectroscopy, and x-ray diffraction (XRD) analysis performed on selected samples; the strain values are in agreement with those obtained by means of standard XRD k-space map analysis.[13]

The knowledge of both x and $\varepsilon_{\parallel}$ has allowed us to calculate the in-plane lattice parameter $a_{\parallel}$ and the equivalent composition x_{eq} of a relaxed cubic alloy with the same lattice constant, which is listed in Table I. In particular, we point out that wells and barriers are always found to be lattice matched $a_{\parallel}$(well)$=a_{\parallel}$(barrier) and also coherent with the underlying

VS. The values obtained for $a_{\parallel}$, correspond to a relaxed bulk alloy with $x_{eq} = 0.93 - 0.95$ (see Table I) suggesting that the VS is not completely plastically relaxed ($x = 0.85$). We can conclude that the SiGe barriers and the Ge wells have a residual average strain of 4.2×10^{-3} and -2.5×10^{-3}, respectively. This incomplete relaxation is almost independent of the thickness of the VS topmost Si$_{0.15}$Ge$_{0.85}$ (in the 350–1000 nm range) and could be related to two different mechanisms. The VS Si$_{0.15}$Ge$_{0.85}$ layer experiences a tensile strain greater than what expected due to its larger thermal expansion coefficient with respect to that of the Si substrate.[13] On the other hand, Shah *et al.*[14,15] have recently reported an incomplete relaxation in reverse graded VS with final composition very similar to the one here studied. They have attributed this effect to the formation of stacking faults in the tensile strain relaxation process which hinder the motion of threading dislocation arms.

B. Optical properties

Low-temperature interband absorption measurements have been performed at normal incidence on the undoped samples listed in Table I. At the absorption edge, the most relevant features in the spectrum are related to transitions in a neighborhood of the Γ point from confined heavy (HH$_i$)- and light (LH$_i$)-hole valence states to conduction states (cΓ_j) with the same subband indices, the optical coupling between subbands with different indices being suppressed by parity selection rule.[26] As an example, the absorbance spectra of sample 1638 measured at $T = 10$ and 77 K are shown in Fig. 4. Strong interband transition peaks, typical of confined excitons, are clearly visible in the spectra pointing to a type I band alignment profile. In particular, consistently with reported results on similar MQW systems,[16–18] HH$_1$-cΓ_1,
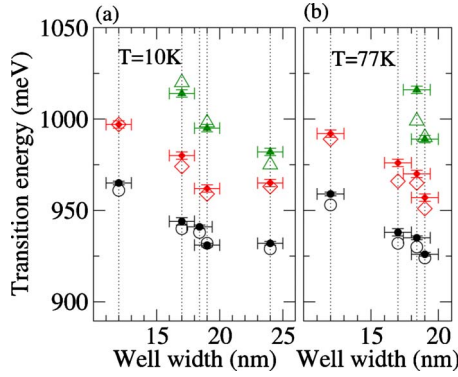
FIG. 5. (Color online) Experimental (filled symbols with error bars) and theoretical (open symbols) HH_1-$c\Gamma_1$ (circles), LH_1-$c\Gamma_1$ (diamonds), and HH_2-$c\Gamma_2$ (triangles) transition energies for the undoped samples of Table I at (a) $T=10$ K and (b) $T=77$ K. The theoretical data report the bare interband transition energy minus the exciton binding energy (see text). Note that the data refer to samples with different parallel lattice constants.

LH_1-$c\Gamma_1$, and HH_2-$c\Gamma_2$ excitonic peaks are well resolved. Similar results are observed for all the investigated samples. The measured absorption energies are reported in Fig. 5 (filled symbols). Peak attribution is supported by theoretical results, obtained by means of a well established TB Hamiltonian model[27] (details are reported in the following Sec. IV).

Low-temperature intersubband-transition absorption spectra have been measured on the doped samples of Table I. The linear dichroic spectra of some of the investigated samples are shown in Fig. 6 in the energy range where intersubband transitions are expected from numerical calculations. Although in this region several absorption lines are observed in the T_M and T_E spectra, the dichroic signal is characterized by a single pronounced transmission dip which is due to a reduced transmission of the TM mode and which monotonically blueshifts upon decreasing the well width. We attribute this feature to optical transitions from the ground to the first excited subband state at the L point. Depending on the number of periods in the MQW structure, on the waveguide length, and on the density of charges transferred in the wells, the observed transmission varies in the 50–90 % range. For the investigated well widths (8.5–24.0 nm) the intersubband transition energies cover the 22–50 meV energy interval. The typical absorption line width [full width at half maximum (FWHM)] is about 10 meV with a maximum of 13.5 meV obtained in the sample 1630.

For the adopted waveguide geometry the dimensionless absorption coefficient $\alpha_{2D}(E)$, associated to each QW, can be evaluated from the transmission data using the relation,[21]

$$\alpha_{2D}(E) = \frac{-\ln[T(E)]\cos(\theta)}{CMN_w \sin^2(\theta)}, \qquad (2)$$

where N_w is the number of QWs in the sample, M is the number of internal reflections in the waveguide, $\theta=45°$ is the angle between the incident radiation and the growth direction, and C is a parameter between 1 and 2 which accounts for the field enhancement due to the surface metallization.
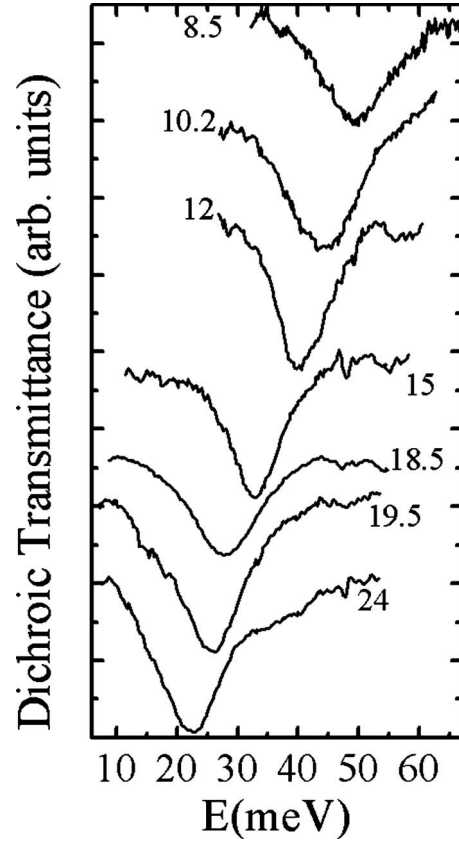

FIG. 6. Dichroic transmittance spectra measured for some of the n-doped Ge/SiGe MQWs with different well width (reported in nanometer).

The α_{2D} spectra of three representative samples obtained from transmittance data using Eq. (2) are reported in Fig. 7. We have used the value $C=1.5$ since this value well reproduces the absorption spectra we have previously measured[8] in s-Si MQW samples with the same waveguide geometry and known electron density in the well, obtained from Hall-effect measurements.

Following the scheme of Refs. 21 and 28, the energy integral of the low-temperature dimensionless absorption coefficient $\alpha_{2D}(E)$ can be related to the two-dimensional (2D)
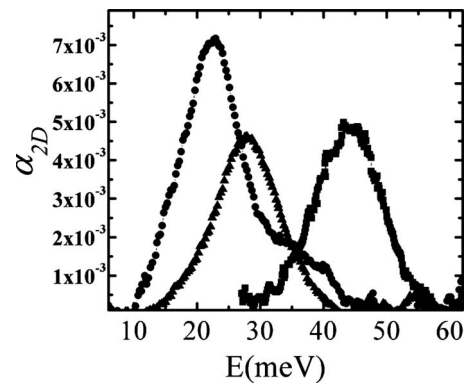

FIG. 7. Single well dimensionless absorption coefficient (see text) for selected samples of Table I: 1598 (circles); 1594 (triangles); and 1616 (squares).

TABLE II. Well widths (d_w) and 2D doping concentrations in the barriers ($\tilde{n}_{2D}=N_D \cdot d_b$) for the doped samples listed in Table I. Measured values at $T=10$ K for the two-dimensional carrier densities transferred into the well region (n_{2D}), the intersubband absorption energies (E_{abs}), and the FWHM (2γ) of the absorption peaks, are also reported.

Sample	d_w (nm)	$\tilde{n}_{2D}10^{12}$ cm$^{-2} \pm 15\%$	$n_{2D}10^{11}$ cm$^{-2} \pm 20\%$	$E_{abs} \pm 1.5$ (meV)	FWHM ± 1 (meV)
1617	8.5	12	1.5	49.5	13
1630	10.0	1.9	1.4	45.5	13.5
1616	10.2	5.5	3.4	46.0	11.5
1619	12.0	11	2.2	39.7	10.5
1596	15.0	14	1.8	32.8	10.5
1594	18.5	12	3	28.1	11
1597	19.5	15	3.9	26.2	9.5
1598	24.0	15	4.7	22.2	10.5

carrier density in the well n_{2D} through the relation:

$$\int \alpha_{2D}(E)dE = \frac{\pi n_{2D}e^2\hbar}{2\eta\varepsilon_0 cm_z}f_{12}, \tag{3}$$

which holds under the assumption that carriers populate only the ground subband and for electric fields oriented along the growth direction; in the above expression $\eta=4$ is the static Ge refractive index, $m_z=0.12m_0$ is the (001) confinement effective mass of the L valley electrons and f_{12} is the dimensionless oscillator strength.

The n_{2D} carrier density of our samples evaluated from Eq. (3) assuming $f_{12}=1$ is reported in Table II. The used value for the oscillator strength is compatible with the values obtained by our numerical calculations, which for the investigated sample are in the 0.92–0.98 range.

We find that the n_{2D} is in the range $1.5–5\times10^{11}$ cm^{-2}. Comparing the n_{2D} values with the 2D donor concentrations $\tilde{n}_{2D}$ reported in Table II, we deduce that most of the donor electrons are not transferred into the wells.

IV. THEORETICAL ANALYSIS AND DISCUSSION

The interband absorption data have been interpreted by means of a tight-binding model for the electronic states, which has proven to be an accurate theoretical tool for the description of SiGe heterostructures (see for instance Refs. 17 and 27). In fact this atomistic approach allows taking into account the geometric details of the whole structure, the chemical composition of the substrate and of the deposited materials, the strain within each layer and the spin-orbit coupling. Starting from a TB parametrization of the electronic states in bulk Si and Ge crystals,[29] the TB model provides an accurate description of valence- and conduction-band electronic states of the SiGe multilayer structures throughout the complete Brillouin zone as well as of their optical properties (details of the model are reported in Ref. 30).

The near gap states and the interband absorption spectra are evaluated using the values listed in Table I as input parameters. An example of the results is given in Fig. 4 where the experimental absorbance spectrum of the sample 1638 is

compared with the corresponding absorption spectrum evaluated at low temperature, considering also excitonic effects with a binding energy of 3.6 meV and a Lorentzian line shape broadening with half width at half maximum equal to $\gamma=5$ meV.[17] The low-temperature Γ-point confined states of sample 1638 are shown in Fig. 8, together with the valence (HH, LH) and the conduction-band edge profiles (the split-off band is lower in energy and is not shown). Note that in the well region the HH band edge is higher in energy than the LH one while the opposite holds for the barriers since the well (barrier) material is compressively (tensile) strained.

The experimental and the theoretical transition energies for samples of different well width are shown in Figs. 5(a) and 5(b). The evaluated transition energies at $T=77$ K [Fig. 5(b)] have been obtained from the low-temperature ones by means of a rigid shift calculated following Ref. 31 to account for the temperature dependence of the direct band gap in Ge
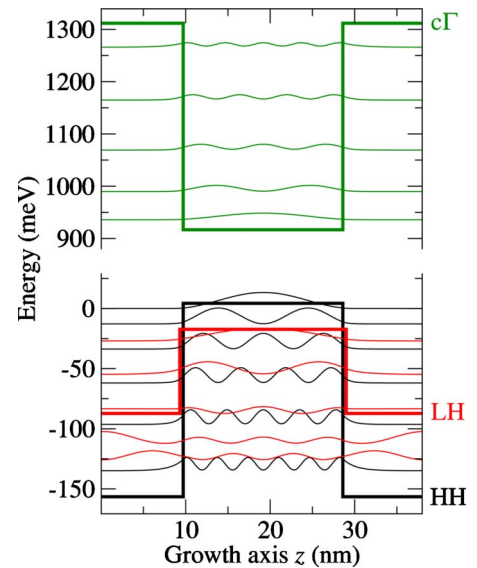

FIG. 8. (Color online) HH (black), LH (red), and cΓ (green) band edge profiles for the sample 1638. The zero of energy is set at the HH$_1$ level. The square moduli of the near-gap wave functions are also shown.

QWs. We notice that deviations from a monotonically decreasing behavior of the absorption energies versus the well width in Fig. 5 are to be attributed to the slightly different parallel lattice constants in the samples, which strongly influence the direct gap of the well material.

The theoretical results reproduce very closely the experimental data. This good agreement demonstrates the validity of the adopted model. Moreover, since the transition energies are very sensitive to the strain field, the results also confirm the accuracy of the strain measurements obtained from the Raman spectra.

We now focus on the analysis of the results obtained from intersubband transitions on the n-doped samples of Table I. An important experimental result is the apparent ineffectiveness of induced charge transfer in these heterostructures.

To understand quantitatively why only a small fraction of the donor electrons in the barriers transfers into the well region, a self-consistent multiband calculation, which takes into account the L, Δ, and Γ conduction valleys, is needed, since these conduction-band minima have very close energies in the heterostructures we have investigated. In this way, partial ionization of the dopants can be properly taken into account for a consistent evaluation of the Fermi energies and of the electronic carrier densities in the wells. The TB formalism is suitable to this goal but it requires quite demanding computations. Consequently, in this work, we have developed a faster multiband self-consistent code in the parabolic $\boldsymbol{k} \cdot \boldsymbol{p}$ envelope function approximation.

In this model the band alignments of the L, Δ, and Γ conduction minima between a biaxially strained $Si_{1-x}Ge_x$ layer grown on a relaxed $Si_{1-y}Ge_y$ substrate are evaluated according to Ref. 32

$$E_c^{L,\Delta,\Gamma}(x,y) = E_{v,avg}(x,y) + \frac{1}{3}\Delta_0(x) + E_g^{L,\Delta,\Gamma}(x) + E_h^{L,\Delta,\Gamma}(x,y)$$
$$+ E_u^{L,\Delta,\Gamma}(x,y), \qquad (4)$$

where $E_g^{L,\Delta,\Gamma}(x)$ are the band gaps at the L, Δ, and Γ points, $\Delta_0(x)$ is the spin-orbit splitting of the unstrained bulk $Si_{1-x}Ge_x$ alloy; $E_h^{L,\Delta,\Gamma}(x,y)$ is the band-gap shift due to the hydrostatic component of the strain, and $E_u^{L,\Delta,\Gamma}(x,y)$ is the contribution from the uniaxial part. $E_{v,avg}(x,y)$ is the offset between the barycenters of the heavy, light, and split-off valence bands in the substrate and in the strained layer and is given by the relation,[33]

$$E_{v,avg}(x,y) = (0.47 - 0.06y)(x - y) \text{ eV.} \qquad (5)$$

The $E_g^{L,\Delta,\Gamma}(x)$ band gaps (in electron volt) for unstrained $Si_{1-x}Ge_x$ alloys are parametrized to reproduce the experimental data according to Ref. 34

$$E_g^L(x) = 2.01 - 1.27x,$$

$$E_g^\Delta(x) = 1.155 - 0.43x + 0.206x^2,$$

$$E_g^\Gamma(x) = 3.37 - 2.48x.$$

Finally, for the hydrostatic, $E_h^{L,\Delta,\Gamma}(x,y)$, and the uniaxial, $E_u^{L,\Delta,\Gamma}(x,y)$, strain terms for the well and barrier regions, it holds[32]

TABLE III. Elastic constants C_{11} and C_{12}, spin-orbit splitting Δ_0 and deformation potentials for Si and Ge bulk crystals adopted in the simulations. Values for SiGe alloys have been obtained by linear interpolation.

	Silicon	Germanium
C_{11} (10^7 N cm^{-2})	1.675[a]	1.315[a]
C_{12} (10^7 N cm^{-2})	0.65[a]	0.494[a]
Δ_0 (eV)	0.044[a]	0.296[a]
$a_c^L - a_v$ (eV)	−3.12 [b]	−2.78 [b]
$a_c^\Delta - a_v$ (eV)	1.72[b]	1.31[b]
Ξ_u^Δ (eV)	8.7[c]	9.42[c]

[a]Data from Ref. 6.
[b]Data from Ref. 32.
[c]Data from Ref. 38.

$$E_h^{L,\Delta,\Gamma}(x,y) = (a_c^{L,\Delta,\Gamma} - a_v) \cdot (2\varepsilon_\parallel + \varepsilon_\perp),$$

$$E_u^{\Delta_2}(x,y) = \frac{2}{3}\Xi_u^\Delta \cdot (\varepsilon_\perp - \varepsilon_\parallel),$$

$$E_u^{\Delta_4}(x,y) = -\frac{1}{3}\Xi_u^\Delta \cdot (\varepsilon_\perp - \varepsilon_\parallel),$$

$$E_u^L(x,y) = E_u^\Gamma(x,y) = 0,$$

where $\varepsilon_\parallel$ and $\varepsilon_\perp$ are the strain components along the parallel and growth directions, respectively; a_c, a_v, and Ξ are the deformation potentials. To take into account the z dependence of the longitudinal and perpendicular effective masses of the strained SiGe and Ge materials, we use the mass parametrization reported in Ref. 33 for Δ and L electrons. Densities of states (DOSs) for the confined states are calculated in the parabolic band approximation with m_{DOS}^L, $m_{DOS}^{\Delta_2}$ and $m_{DOS}^{\Delta_4}$ given by[35]

$$m_{DOS}^L = \sqrt{m_t^L \cdot \frac{m_t^L + 2m_l^L}{3}}, \quad m_{DOS}^{\Delta_2} = m_t^\Delta, \quad m_{DOS}^{\Delta_4} = \sqrt{m_t^\Delta \cdot m_l^\Delta},$$

where m_l^L (m_l^Δ) and m_t^L (m_t^Δ) are the longitudinal and transverse L (Δ) effective masses, respectively.

The values adopted for some relevant parameters are summarized in Table III for Si and Ge bulk crystals. The corresponding parameters for the SiGe barrier material are obtained by linear interpolation. Nonlinear interpolations are instead adopted for the lattice constant[36] and the static refractive index.[37]

The electronic states are calculated self-consistently in the Schrödinger-Poisson iterative scheme, taking into account ionized impurities, and contributions to the Hartree potential from electrons at the L, Δ, and Γ valleys. Exchange-correlation effects are included in the local-density approximation[39] only for the 2D electrons at the L point since at low temperature the free electron density is mostly due to the confined carriers at L. The Fermi level E_f is evaluated as a function of temperature taking into account also the occupation of the impurity levels in the barriers. We assume
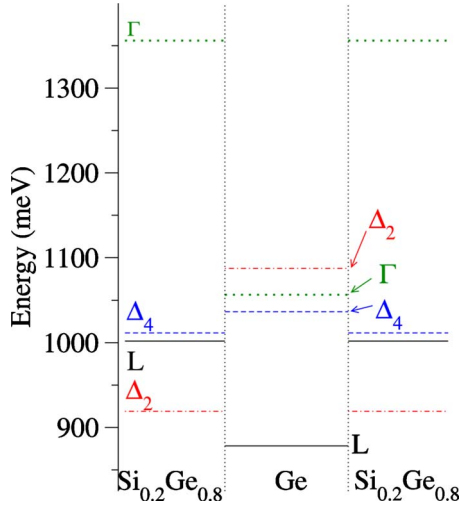
FIG. 9. (Color online) L (black, solid), Δ_2 (red, dotted-dashed), Δ_4 (blue, dashed), and Γ (green, dotted) conduction-band edge profiles for the investigated Ge/Si$_{0.2}$Ge$_{0.8}$ QW structures on (001) relaxed Si$_{0.07}$Ge$_{0.93}$ substrates. The zero of energy is set at the average of the valence bands in the substrate.

FIG. 10. (Color online) L (black) and Δ_2 (red) band profiles and squared wave functions for the 1594 sample calculated at T = 10 K. The green shaded region of width $4kT$ is centered on the Fermi energy. The donor level in the barriers is represented by a blue dashed line.

that the energies of the impurity states are E_b meV below the z-dependent conduction minimum of the barrier material; we adopt for E_b the value of the binding energy of phosphorus in a Si$_{0.2}$Ge$_{0.8}$ bulk alloy (see Refs. 22 and 40). Moreover, the occupancy of bound impurity states is evaluated avoiding double occupation due to Coulomb repulsion.[41]

The obtained L, Δ_2, Δ_4, and Γ conduction-band edge profiles are shown in Fig. 9. The in-plane compressive (tensile) strain in the well (barrier) region moves upward (downward) the Δ_2 states while the opposite holds for the Δ_4 levels. Note also that for (001) biaxially strained layers the four L valleys remain degenerate. From Fig. 9 it is evident that the conduction minimum in the doped barrier material, where the donor levels are located, is along the Δ_2 lines. The Γ and Δ_4 states are higher in energy and thus at low temperature are expected to play a negligible role for charge redistribution. We find that the band offset between the L edges is 124 meV and the energy difference between the Δ_2 minima in the barrier and the L minima in the well is only ~40 meV.

The results of the self-consistent calculation for the conduction electronic states at 10 K in the sample 1594 are reported in Fig. 10. The dashed line at about 25 meV below the Δ_2 band edge represents the donor level. The Fermi energy is also shown. Note that far from the interfaces the donor level in the barriers is below the Fermi energy. As a consequence a very small fraction of the donor impurity states is ionized. In other words the electronic density in the well due to the transfer doping is limited by the small energy difference between the Δ_2 minima in the barrier and the L minima in the well. The two-dimensional carrier densities for the *n*-doped samples of Table I are reported in Fig. 11(a) for samples having different well widths.

Measured (closed symbols) as well as calculated (open) n_{2D} values are both in the range $1-5\times10^{11}$ cm^{-2}. We point here out that the absence of a general trend of the n_{2D} values as a function of the well width is to be attributed to the
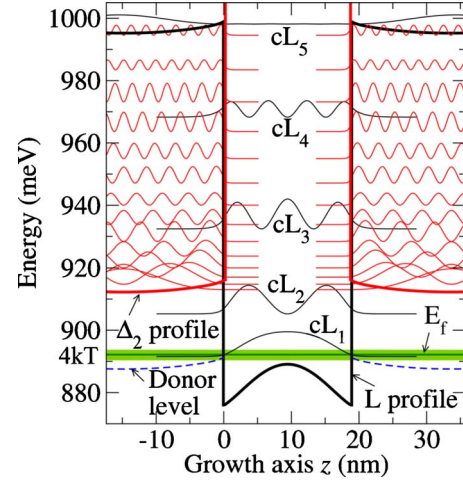
different doping levels and geometries of the samples. For instance, as expected, the insertion of a spacer between the well and the doped barrier region [triangles in Figs. 11(a) and 11(b)] reduces the charge transferred into the well, despite their larger number of donors with respect to the samples
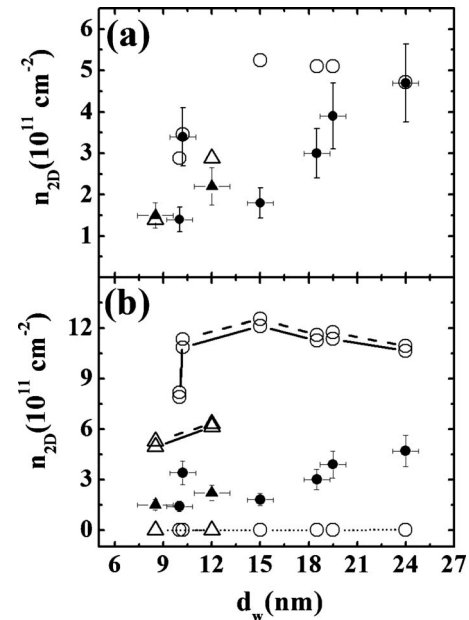

FIG. 11. (a) Measured (closed symbols) and calculated (open symbols) two-dimensional carrier densities, n_{2D}, in the well region plotted as a function of the well width for the *n*-doped samples of Table I. Calculations have been carried out using the parameter values reported in Table III. (b) Two-dimensional carrier densities as measured (closed symbols) and calculated (open symbols) modifying the parameter values of Table III as follows: Ξ_u^Δ=5 eV (dashed line); $\Delta E_{v,avg}$=0.060 eV (solid line); and $\Delta E_{v,avg}$=0.104 eV (dotted line). Samples with spacer layers (1617 and 1619) are represented by triangles.

with similar well width. The overall agreement between the predicted and the measured values of n_{2D} is satisfactory.

The discrepancies between theoretical and measured densities observed in Fig. 11(a) for some of the investigated samples may be mainly attributed to the unavoidable uncertainties affecting their compositional and structural parameters, in particular, those related to the precise evaluation of the Δ_2-L energy separation. In fact our simulations indicate that the amount of charge transferred into the well region critically depends on the energy difference between the L and Δ_2 conduction valleys in the well and barrier materials, respectively. As an example, for the sample 1596 (whose calculated n_{2D} is 5.2×10^{11} cm^{-2}), the experimental value $n_{2D} = 1.8 \times 10^{11}$ cm^{-2} is exactly reproduced decreasing the Δ_2-L energy difference by only 8 meV. This small change in the Δ_2-L separation can be for instance related to a variation in the Ge content in the barrier from 80% to 79%, a quantity which is within our experimental uncertainty.[13]

From the measured carrier densities we deduce that only the lowest (E_1) conduction subband is populated at low temperature. This confirms that the measured absorption peaks are related to the $E_1 \rightarrow E_2$ transitions at the L point in the Ge region. Neglecting the minor contribution due to the excitonic interaction, and in the two-level model,[20] the energy of the absorption resonance E_a is given by

$$E_a^2 = E_{21}^2 (1 + \alpha),$$

where E_{21} is the bare intersubband transition energy and $\alpha = \frac{2e^2 n_{2D}}{\varepsilon \varepsilon_0 E_{21}} S$ accounts for the blueshift induced by the depolarization effect. S is an effective length given by

$$S = \int_{-\infty}^{\infty} dz \left[\int_{-\infty}^{z} dz' \, \psi_2(z') \psi_1(z') \right]^2$$

and ψ_1 and ψ_2 are the ground and first excited L subband wave functions, respectively.

In Fig. 12(a) we compare the theoretical evaluation of the intersubband absorption energies with the corresponding measured values. We observe that the theoretical model satisfactory reproduces the measured data, especially for small d_w where depolarization effects are negligible and the transition energy is more sensitive to the conduction-band offset.[8] Note however that in the large well region, absorption energies are systematically underestimated.

In the investigated samples the Hartree potential and the plasmon effect are responsible of significant deviations of the intersubband absorption resonances from the bare intersubband transition energies as calculated in the flat band approximation. These two effects cannot be separated and depend on the amount of charge transferred into the well region. On the other hand, since the n_{2D} carrier densities in the well depend critically on the Δ_2-L energy differences, besides the uncertainties related to the structural and chemical composition of the samples, also those affecting the other input parameters used in the model play an important role in the calculated n_{2D} values. Indeed, several material parameters jointly contribute to determine the Δ_2-L energy difference, as for instance the hydrostatic and uniaxial deformation potentials of Δ states in Ge, for which no experimental val-
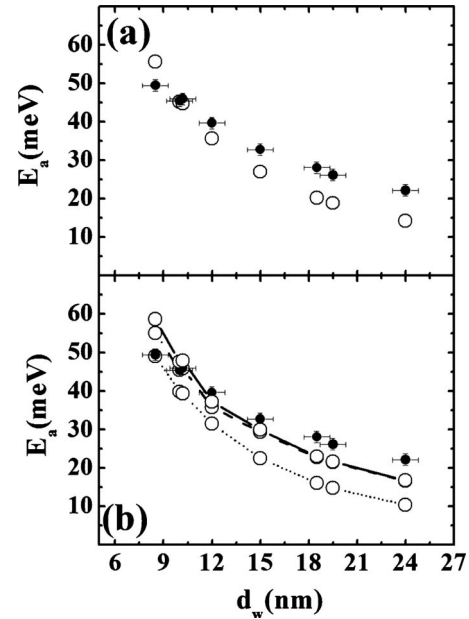

FIG. 12. (a) Measured (closed symbols) and calculated (open symbols) intersubband absorption energies as a function of the quantum well width d_w. Calculations have been carried out using the parameter values reported in Table III. (b) Intersubband absorption energies as measured (closed symbols) and calculated (open symbols) modifying the parameter values of Table III as follows: $\Xi_u^\Delta = 5$ eV (dashed line); $\Delta E_{v,avg} = 0.060$ eV (solid line); and $\Delta E_{v,avg} = 0.104$ eV (dotted line).

ues are reported in the literature, or the valence-band offsets $\Delta E_{v,avg}$ of the strained SiGe interface, whose precise values are still under debate.[42,43] For this reason one can think to tune within the known uncertainty a subset of the model parameters in order to simultaneously fit the numerical results with the measured n_{2D} densities and intersubband absorption energies. In this way the model could be exploited to suggest more precise values for these fitting material parameters. However, we found that the introduction of one fitting parameter in the model does not led to a substantially better agreement between measured and calculated absorption energies. More precisely, if the Δ_2-L energy difference is increased, higher absorption energies in the large well region are found due to the enhancement of the plasmonic blueshift. Nevertheless, for reasonably values of the fitting parameter, this improvement remains modest while the evaluated 2D carrier densities significantly change. As a consequence the good agreement previously obtained with the measured densities is lost.

Among the different material parameters which influence the Δ_2-L energy difference, we have tested as fitting variables the Ξ_u^Δ deformation potential for Ge and the $\Delta E_{v,avg}$ valence offset, due to the relatively large indetermination which affect them. As one can easily get convinced, larger Δ_2-L energy differences can be obtained if smaller values of Ξ_u^Δ (Ge) or $\Delta E_{v,avg}$ are assumed.

As an example in Fig. 12(b) (dashed line) numerical absorption energies calculated diminishing the uniaxial deformation potential Ξ_u^Δ of Ge to the tentative fit value of 5 eV are reported. In this case the Δ_2 donor states have higher

energies and the carrier densities become 2–4 times larger than the measured ones, as reported in Fig. 11(b) but the improvement in the energy differences between the measured and calculated absorption energies for the large well region is only on the order of 5%. We point out that the relative insensitiveness of the absorption energies with respect to n_{2D} in the 10^{11}–10^{12} cm^{-2} density range here investigated, can be attributed to the opposite sign of the Hartree potential and the plasmonic effect contributions to the absorption energies.

Similar results are found if the barycenter valence-band offset between the well and barrier materials $\Delta E_{v,avg}$ is decreased from the value of 0.083 eV, obtained by means of Eq. (5), to the tentative fit value of 0.060 eV [see Figs. 11(b) and 12(b), solid lines].

For the sake of completeness we also report in Fig. 12(b) (dotted line) absorption energies obtained with a larger $\Delta E_{v,avg}$. In this case the Δ_2-L difference diminishes and then the amount of transferred charge rapidly decreases. For instance at $\Delta E_{v,avg}=0.104$ eV, a value calculated according to the relation for the offsets between the *topmost* valence bands given in Ref. 42, n_{2D} are less than 10^{10} cm^{-2} [see Fig. 11(b)]. Therefore the absorption resonances, which are now practically coincident with the flat band transition energies, become even more underestimated [see Fig. 12(b)].

In summary, the use of material parameters as fitting variables of the model does not remove the small systematic deviation between measured and calculated intersubband absorption energies observed in the large well width region. Then we conclude that from the present experiments there is no evidence to invoke new values for the material parameters since the literature data [see Table III and Eq. (5)] allows a sound theoretical description of the measurements. The discrepancy in the absorption energies found for the large well samples could be more profitably addressed by means of first-principles calculations which however are beyond the scope of this work. In fact, it is well known that when the collective (plasmon) energies become as large as E_{21}, as it happens for the investigated samples with large wells, the intersubband resonances cannot be described in a single-particle framework anymore.[21]

V. CONCLUSIONS

High-quality s-Ge/Si$_{0.2}$Ge$_{0.8}$ multiquantum well structures having low interface roughness (<0.4 nm) and threading dislocation density ($\sim10^6$–10^7 cm^{-2}) have been grown by UHV-CVD on reverse Si$_{0.15}$Ge$_{0.85}$/Si(001) virtual substrates. Raman measurements have shown that wells and barriers are lattice matched and have a residual average strain of $\varepsilon_{bar}=4.2\times10^{-3}$ and $\varepsilon_{well}=-2.5\times10^{-3}$, respectively. NIR absorption measurements exhibit well-defined interband HH$_1$-cΓ_1, LH$_1$-cΓ_1, and HH$_2$-cΓ_2 transition peaks, typical of confined excitons, pointing to a type I band alignment profile.

Far infrared absorption spectra performed on *n*-doped samples are characterized by a single pronounced peak attributed to transitions from the ground to the first excited conduction subband. This peak blueshifts upon decreasing the well width. For the investigated well width range (8.5–24.0 nm) the intersubband absorption energies are in the 22–50 meV range. The analysis of the absorption spectra indicated n_{2D} carrier densities in the s-Ge wells ranging from 1.5×10^{11} to 5×10^{11} cm^{-2}, evidencing an incomplete transfer of the electrons from the P donors in the SiGe barriers.

Interband and intersubband transition energies have been successfully modeled using tight binding and $\boldsymbol{k}\cdot\boldsymbol{p}$ calculations, providing the electronic band structure of the complete MQW structure throughout the whole Brillouin zone. The agreement between theoretical and experimental data demonstrates the effectiveness of the adopted theoretical models for evaluating band profile and electronic structures. In particular, we found that the conduction-band offset at the L point is 124 meV, a value well suited for the development of optoelectronic devices operating in the THz range. Moreover, we found an energy difference between the Δ_2 minima in the barrier and the L minima in the well of ~40 meV only. This could account for the observed ineffectiveness of doping charge transfer in these strained heterostructures.

*Corresponding author; capellini@fis.uniroma3.it

[1] D. J. Paul, Semicond. Sci. Technol. **19**, R75 (2004).

[2] M. Virgilio and G. Grosso, J. Appl. Phys. **100**, 093506 (2006).

[3] M. Virgilio and G. Grosso, J. Phys.: Condens. Matter **18**, 1021 (2006).

[4] K. Driscoll and R. Paiella, Appl. Phys. Lett. **89**, 191110 (2006).

[5] M. De Seta, G. Capellini, Y. Busby, F. Evangelisti, M. Ortolani, M. Virgilio, G. Grosso, G. Pizzi, A. Nucara, and S. Lupi, Appl. Phys. Lett. **95**, 051918 (2009).

[6] F. Schäffler, Semicond. Sci. Technol. **12**, 1515 (1997).

[7] H. Hertle, G. Schuberth, E. Gornik, G. Abstreiter, and F. Schäffler, Appl. Phys. Lett. **59**, 2977 (1991).

[8] G. Ciasca, M. De Seta, G. Capellini, F. Evangelisti, M. Ortolani, M. Virgilio, G. Grosso, A. Nucara, and P. Calvani, Phys. Rev. B **79**, 085302 (2009).

[9] S. A. Lynch, R. Bates, D. J. Paul, D. J. Norris, A. G. Cullis, Z. Iconic, R. W. Kelsall, P. Harrison, D. D. Arnone, and C. R. Pidgeon, Appl. Phys. Lett. **81**, 1543 (2002).

[10] R. Bates, S. A. Lynch, D. J. Paul, Z. Ikonic, R. W. Kelsall, P. Harrison, S. L. Liew, D. J. Norris, and A. G. Cullis, Appl. Phys. Lett. **83**, 4092 (2003).

[11] G. Matmon, D. J. Paul, L. Lever, M. Califano, Z. Ikonić, R. W. Kelsall, J. Zhang, D. Chrastina, G. Isella, H. von Känel, E. Müller, and A. Neels, J. Appl. Phys. **107**, 053109 (2010).

[12] B. Rössner, D. Chrastina, G. Isella, and H. von Känel, Appl. Phys. Lett. **84**, 3058 (2004).

[13] G. Capellini, M. De Seta, Y. Busby, M. Pea, F. Evangelisti, G. Nicotra, C. Spinella, M. Nardone, and C. Ferrari, J. Appl. Phys. **107**, 063504 (2010).

[14] V. A. Shah, A. Dobbie, M. Myronov, D. J. F. Fulgoni, L. J. Nash, and D. R. Leadley, Appl. Phys. Lett. **93**, 192103 (2008).

[15] V. A. Shah, A. Dobbie, M. Myronov, and D. R. Leadley, J. Appl. Phys. **107**, 064304 (2010).

[16] S. Tsujino, H. Sigg, G. Mussler, D. Chrastina, and H. von Känel, Appl. Phys. Lett. **89**, 262119 (2006).

[17] M. Bonfanti, E. Grilli, M. Guzzi, M. Virgilio, G. Grosso, D. Chrastina, G. Isella, H. von Känel, and A. Neels, Phys. Rev. B **78**, 041407(R) (2008).

[18] M. Virgilio, M. Bonfanti, D. Chrastina, A. Neels, G. Isella, E. Grilli, M. Guzzi, G. Grosso, H. Sigg, and H. von Känel, Phys. Rev. B **79**, 075323 (2009).

[19] C. Lange, N. S. Köster, S. Chatterjee, H. Sigg, D. Chrastina, G. Isella, H. von Känel, M. Schäfer, M. Kira, and S. W. Koch, Phys. Rev. B **79**, 201306(R) (2009).

[20] Y.-H. Kuo, Y. K. Lee, Y. Ge, S. Ren, J. E. Roth, T. I. Kamins, D. A. B. Miller, and J. S. Harris, Nature (London) **437**, 1334 (2005).

[21] M. Helm, in *Intersubband Transitions in Quantum Wells: Physics and Device Applications I*, edited by H. C. Liu and F. Capasso (Academic Press, New York, 2000).

[22] M. Franz, K. F. Dombrowski, H. Rücker, B. Dietrich, K. Pressel, A. Barz, U. Kerat, P. Dold, and K. W. Benz, Phys. Rev. B **59**, 10614 (1999).

[23] J. C. Tsang, P. M. Mooney, F. Dacol, and J. O. Chu, J. Appl. Phys. **75**, 8098 (1994).

[24] F. Pezzoli, E. Grilli, M. Guzzi, S. Sanguinetti, D. Chrastina, G. Isella, H. Von Känel, E. Wintersberger, J. Stangl, and G. Bauer, Mater. Sci. Semicond. Process. **9**, 541 (2006).

[25] F. Pezzoli, E. Bonera, E. Grilli, M. Guzzi, S. Sanguinetti, D. Chrastina, G. Isella, H. Von Känel, E. Wintersberger, J. Stangl, and G. Bauer, J. Appl. Phys. **103**, 093521 (2008).

[26] G. Bastard, *Wave Mechanics Applied to Semiconductor Heterostructures* (Wiley-Interscience, Bognor Regis, 1991).

[27] G. Pizzi, M. Virgilio, and G. Grosso, Nanotechnology **21**, 055202 (2010).

[28] E. R. Brown and S. J. Eglash, Phys. Rev. B **41**, 7559 (1990).

[29] J. M. Jancu, R. Scholz, F. Beltram, and F. Bassani, Phys. Rev. B **57**, 6493 (1998).

[30] M. Virgilio and G. Grosso, Phys. Rev. B **77**, 165315 (2008).

[31] Y. Yin, D. Yan, F. H. Pollak, M. S. Hybertsen, J. M. Vandenberg, and J. C. Bean, Phys. Rev. B **52**, 8951 (1995).

[32] C. G. Van de Walle and R. M. Martin, Phys. Rev. B **34**, 5621 (1986).

[33] M. M. Rieger and P. Vogl, Phys. Rev. B **48**, 14276 (1993).

[34] J. Weber and M. I. Alonso, Phys. Rev. B **40**, 5683 (1989).

[35] F. Stern and W. E. Howard, Phys. Rev. **163**, 816 (1967).

[36] J. P. Dismukes, L. Ekstrom, and R. J. Paff, J. Phys. Chem. **68**, 3021 (1964).

[37] D. J. Paul, Laser Photonics Rev. **4**, 610 (2010).

[38] C. G. Van de Walle, Phys. Rev. B **39**, 1871 (1989).

[39] O. Gunnarsson and B. I. Lundqvist, Phys. Rev. B **13**, 4274 (1976).

[40] R. Krüssmann, H. Vollmer, and R. Labusch, Phys. Status Solidi B **118**, 275 (1983).

[41] G. Grosso and G. Pastori Parravicini, *Solid State Physics* (Academic Press, London, 2000).

[42] V. V. Afanas'ev, A. Stesmans, L. Souriau, R. Loo, and M. Meuris, Appl. Phys. Lett. **94**, 172106 (2009).

[43] S. V. Kondratenko, A. S. Nikolenko, O. V. Vakulenko, M. Ya. Valakh, V. O. Yukhymchuk, A. V. Dvurechenskii, and A. I. Nikiforov, Nanotechnology **19**, 145703 (2008).